

Heterointerface Control over Lithium-Induced Phase Transitions in MoS₂ Nanosheets: Implications for Nanoscaled Energy Materials

Joshua V. Pondick, Aakash Kumar, Mengjing Wang, Sajad Yazdani, John M. Woods, Diana Y. Qiu, and Judy J. Cha*



Cite This: *ACS Appl. Nano Mater.* 2021, 4, 14105–14114



Read Online

ACCESS |

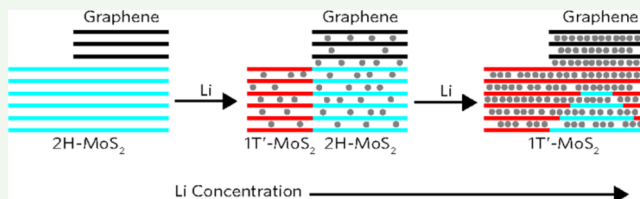
Metrics & More

Article Recommendations

Supporting Information

ABSTRACT: Phase transitions of two-dimensional nanomaterials and their heterostructures enable many applications including electrochemical energy storage, catalysis, and memory; however, the nucleation pathways by which these transitions proceed remain underexplored, prohibiting engineering control for these applications. Here, we demonstrate that the lithium intercalation-induced 2H-1T' phase transition in MoS₂ nanosheets proceeds via nucleation of the 1T' phase at an atomically thin heterointerface by monitoring the phase transition of MoS₂/graphene and MoS₂/hexagonal boron nitride (hBN) heterostructures with Raman spectroscopy *in situ* during intercalation. We observe that graphene–MoS₂ heterointerfaces require an increase of 0.8 V in applied electrochemical potential to nucleate the 1T' phase in MoS₂ as compared to hBN–MoS₂ heterointerfaces. The increased nucleation barrier at graphene–MoS₂ heterointerfaces is due to the reduced charge transfer from lithium to MoS₂ at the heterointerface as lithium also dopes graphene based on *ab initio* calculations. Furthermore, we show that the growth of the 1T' domain propagates along the heterointerface rather than through the interior of MoS₂. Our results provide the first experimental observations of the heterogeneous nucleation and growth of intercalation-induced phase transitions in two-dimensional nanomaterials and heterointerface effects on their phase transitions. These insights have implications for the design of energy technologies and devices that rely upon the phase stability of nanostructured materials.

KEYWORDS: phase transition, heterostructure, lithium intercalation, heterogeneous nucleation, MoS₂, graphene, hBN



INTRODUCTION

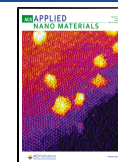
Nucleation phenomena are fundamental to many natural processes and remain a critical area of study in a wide range of fields including protein phase transitions in biology,^{1–4} nucleation of atmospheric particulates in climate science,^{5,6} crystallization dynamics in metals for structural materials,^{7–9} and synthesis of nanomaterials.^{10–12} Phase transitions are initiated by nucleation, and the transition pathways between phases are complex and heavily influenced by factors such as nanoscale confinement and interfaces.¹³ For atomically thin layered transition-metal dichalcogenides (TMDs) that can exist in several structural polymorphs,¹⁴ the phase transitions between these polymorphs have proven important for neuromorphic memristive computing,^{15–17} the production of hydrogen using two-dimensional (2D) nanocatalysts,^{18–22} and nanoscaled logic devices.²³ The phase stability of 2D nanomaterials during intercalation is also essential in their application as nanostructured electrodes for metal-ion batteries.^{24–27} To effectively exploit these phase transitions for these applications, understanding the thermodynamics and kinetics of the nucleation pathways is essential; however, nucleation pathways remain virtually unexplored for many TMDs that have been demonstrated to undergo phase transitions.

For example, despite the well-established phase transition from the semiconducting 2H phase to the semimetallic 1T' phase via lithium intercalation into the TMD MoS₂,^{28–31} the nucleation pathway has not been experimentally studied at the microscopic level. *Ab initio* calculations indicate that the lithium-induced phase transition in MoS₂ is due to the electron doping from intercalated lithium atoms into the conduction band of 2H-MoS₂: at a critical donated electron concentration, the sulfur atoms change their coordination around molybdenum from trigonal prismatic to octahedral, thus forming 1T'-MoS₂.^{32–35} Constructing heterointerfaces by interfacing MoS₂ with other 2D nanomaterials could modulate the charge donation from lithium at the heterointerface, thus enabling the study of nucleation pathways in the lithium-induced 2H-1T' phase transition of MoS₂. Recently, heterointerface effects in the electrochemical intercalation of van der Waals (vdW) heterostructures have been investigated

Received: October 15, 2021

Accepted: November 5, 2021

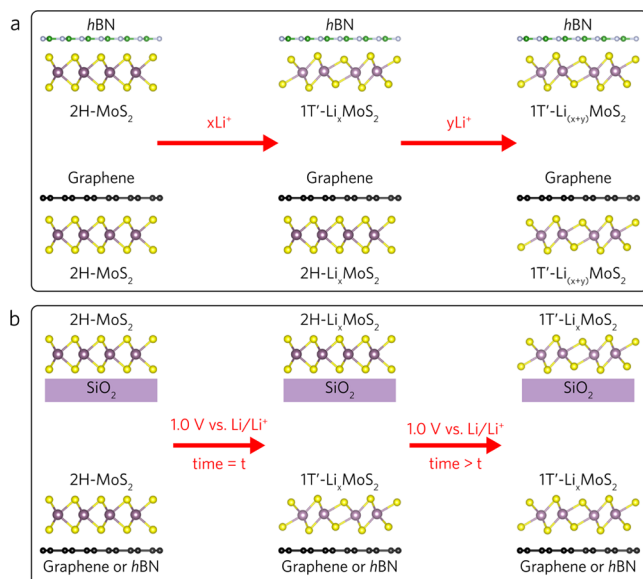
Published: November 17, 2021



to understand how heterointerfaces modulate electron transport and lithium storage.³⁶ However, heterointerface effects on the phase transition, and consequently on the nucleation pathway, have not been examined.

We thus investigate the electrochemical intercalation of lithium into MoS₂/graphene or MoS₂/hexagonal boron nitride (hBN) heterostructures to probe how the heterointerface can modify the 2H-1T' phase transition in MoS₂ (**Scheme 1**).

Scheme 1. Heterointerface Control over Phase Transition Dynamics in MoS₂ Nanosheets^a



^a(a) The identity of the 2D nanosheet covering MoS₂ determines the critical lithium concentration required to induce the 2H-1T' phase transition in a MoS₂ heterostructure. (b) The weak vdW interactions between MoS₂ and a 2D support will facilitate a more rapid 2H-1T' phase transition than when MoS₂ is supported by SiO₂.

Using *in situ* Raman spectroscopy, we demonstrate that the nucleation of the 1T' phase in MoS₂ is heterogeneous and that the heterogeneous nucleation is determined by the top heterointerface. As outlined in **Scheme 1a**, a graphene/MoS₂ interface increases the critical lithium concentration required to nucleate the 1T' phase in MoS₂, while an hBN/MoS₂ interface has no effect on the phase transition. We attribute this behavior to the donation of significant electron density from lithium into graphene at the heterointerface, as predicted by ab initio calculations. **Scheme 1b** illustrates our observation that the support substrate can modify the kinetics of the 2H-1T' phase transition, with a 2D support substrate accelerating the phase transition as compared to a SiO₂ substrate. Post mortem analysis indicates that this kinetic enhancement is due to the weak vdW interactions between MoS₂ and a 2D support that facilitate the release of the mechanical strain developed during the phase transition.

EXPERIMENTAL METHODS

Ab Initio Calculations. Density functional theory (DFT) calculations were carried out using a plane-wave basis set within the projector augmented wave^{37,38} approach using the Quantum Espresso³⁹ software package. The 4s and 4p semi-core states of Mo were included as valence electrons and the exchange–correlation was treated at the generalized gradient approximation level of Perdew–Becke–Ernzerhof.⁴⁰ The vdW interactions were accounted for using

Grimme's D3 dispersion correction.⁴¹ A 4 × 4 MoS₂–5 × 5 graphene supercell was used containing one monolayer of MoS₂ sandwiched between six layers of graphene, where the graphene was strained in-plane by ~1.3% to create a commensurate interface, with zero strain in the direction normal to the interface. The kinetic energy cutoff for the plane waves was set to 1040 eV, and a Gamma-centered Monkhorst-Pack⁴² K-mesh of 8 × 8 × 1 was employed to sample the Brillouin Zone. A Li atom was introduced at the preferred site on top of a Mo atom,⁴³ and all the atoms in the supercell were relaxed until the total energy converged to within 0.2 meV/atom, and the forces on each atom were smaller than 0.03 eV/Å. Bader charge analysis⁴⁴ was carried out on the relaxed equilibrium configuration to determine the change in the charge distribution induced by Li. For freestanding MoS₂, Li donated $-0.88e$ (where e stands for the elementary charge), while in a graphene/MoS₂ heterostructure, Li donated $-0.30e$ to MoS₂, $-0.42e$ to the three graphene layers adjacent to Li, and $-0.16e$ to the bottom graphene layers. For the hBN-MoS₂ heterointerface, a 3 × 3 MoS₂–4 × 4 hBN supercell was used containing one monolayer of MoS₂ and six layers of hBN, where the hBN was strained in-plane by ~4.8% to create a commensurate interface. Further details for the hBN-MoS₂ calculations can be found in our previous work.⁴⁵ Bader charge analysis revealed that for freestanding MoS₂, Li donated $-0.97e$, while in a hBN/MoS₂ heterostructure, Li donated $-0.87e$ to MoS₂ and $-0.1e$ to hBN.

Device Fabrication. Several-layer MoS₂ (SPI Supplies), graphene (NGS Naturgraphit GmbH), and hBN (HQ Graphene) flakes were mechanically exfoliated from bulk crystals onto SiO₂/Si substrates using the scotch-tape method. The substrates were sonicated in acetone and isopropyl alcohol, and treated with O₂ plasma prior to exfoliation. MoS₂ flake thickness was identified via the separation between the E_{2g} and A_{1g} Raman modes^{46,47} measured using Raman spectroscopy (**Figure S1**). Graphene flake thickness was determined via the ratio of the intensity of the Si Raman peak at 520 cm⁻¹ measured through the flake as compared to the intensity of the Si peak measured directly from the substrate, as we previously described.⁴⁸ Raman analysis shows a low defect density in the graphene flakes (**Figure S1**). hBN flake thickness was estimated using optical microscopy.

Flakes of desired size and thickness were transferred to SiO₂/Si substrates using a KOH-assisted technique, as we described previously.^{45,48} Heterostructures were fabricated by repeating the flake transfer and using the micro-manipulator and a rotational stage to carefully control the placement of the second flake on top of the previously transferred bottom flake. All MoS₂ flakes used in this study were 5–7 layers thick, all graphene support flakes were 6–10 layers thick, and all graphene flakes covering MoS₂ were 5 layers thick to minimize the attenuation of the Raman signal from MoS₂.

For electrochemical lithium intercalation, electrodes were patterned with electron beam lithography [Nabity NPGS, Helios G4 FIB-scanning electron microscope (SEM)] and then 10 nm Cr/100 nm Au was thermally deposited (Mbraun EcoVap). For partially covered MoS₂/graphene devices, electrodes were patterned onto both MoS₂ and graphene; for MoS₂ encapsulated by graphene, electrodes were deposited onto both the top and bottom graphene flakes, and for hBN/MoS₂ heterostructures, electrodes were deposited onto MoS₂ only.

Electrochemical Cell Fabrication and Operation. Cr/Au-contacted heterostructures fabricated on SiO₂/Si were integrated into electrochemical microreactors, as described previously.^{49–51} Briefly, the on-chip device is inserted into an airtight cell along with Li metal pressed onto Cu. The cell is filled with a liquid electrolyte containing 1 M lithium hexafluorophosphate in 50/50 v/v ethylene carbonate/diethyl carbonate (LiPF₆ in EC/DEC, Sigma Aldrich), and sealed within an argon glovebox. An optical window is included to allow for *in situ* probing during device operation.

Intercalation cells were connected to a Biological SP300 potentiostat/galvanostat for the electrochemical intercalation of Li⁺. The Cr/Au contacts to the device served as the working electrode, while the lithium/copper served as the reference/counter electrode. In all experiments, working electrodes were connected together to

allow for simultaneous intercalation through all working electrodes. Lithium was intercalated into the heterostructures potentiostatically by dropping the electrochemical potential (V_{EC}) versus Li/Li⁺ at a scan rate of 10 mV s⁻¹ from the open circuit voltage (OCV, ~2.7 V vs Li/Li⁺) to a desired potential. A more detailed description of cell fabrication and operation can be found in our previous work.⁴⁵

Raman Characterization. All Raman spectra were recorded with a Horiba LabRAM HR evolution spectrometer with an 1800 lines/mm diffraction grating. MoS₂ thickness was determined with a 532 nm laser, while graphene thickness and all *in situ* spectra were recorded with a 633 nm laser. *In situ* Raman spectra were recorded with fifteen 5 s exposures. Due to the extremely low Raman signal, hBN could not be characterized during intercalation (Figure S1). Raman spectroscopy was used to monitor the phase of intercalated MoS₂ as it is a noninvasive technique that can sample the phase throughout the entire thickness of the heterostructures with micron-scale spatial resolution. Other characterization techniques such as *in situ* transmission electron microscopy (TEM) are incompatible with liquid electrolytes, while X-ray diffraction or photoelectron spectroscopy conducted on microflakes yield extremely low signals that prevent a meaningful analysis.

Post Mortem Characterizations. Post intercalation, the micro-reactors were opened using a razor blade to remove the epoxy walls to recover the SiO₂/Si on-chip device. Recovered devices were placed into an isopropyl alcohol wash, dried, and then characterized with optical microscopy and Raman spectroscopy. Structural characterization of devices was carried out with SEM (Helios G4 FIB-SEM) at a tilt angle of 0 and 40°.

RESULTS AND DISCUSSION

We investigate the effects of a heterointerface on the phase transition of MoS₂ by considering the lithium intercalation of two heterostructures: graphene–MoS₂ and hBN–MoS₂. Upon lithium intercalation, graphene readily accepts charge from lithium,^{52,53} while insulating hBN is not expected to interact significantly with intercalated lithium.^{45,54} We employed DFT calculations to determine the equilibrium configuration of the graphene–MoS₂ and hBN–MoS₂ heterointerfaces with a Li intercalant, followed by Bader charge analysis to determine how charge from the Li is donated at each heterointerface. As shown in Figure 1, Li donates close to one electron to freestanding MoS₂. Consistent with our previous work,⁴⁵ the amount of charge donated by Li is slightly reduced at the hBN–MoS₂ heterointerface, with 90% of the charge donated to the MoS₂ layer and 10% donated to the hBN. At the graphene–MoS₂ heterointerface; however, we find a dramatic reduction in charge donation from Li to MoS₂, with 34% of the charge transferred to the MoS₂ layer and 48% to the three adjacent graphene layers, and the rest of the charge (~18%) is donated to the bottom three graphene layers (not shown in the schematic in Figure 1b). Density of states calculations show that lithium can dope electrons across a wide range of energies at the MoS₂–graphene heterointerface (Figure S2). Thus, we find that interfacing MoS₂ with graphene lowers the overall charge donated, and hence, the effective doping power of Li to MoS₂ by ~60% when compared to both the MoS₂–hBN heterostructure and freestanding MoS₂.

Motivated by the DFT analysis, we fabricated heterostructures of several-layer MoS₂ interfaced with graphene and hBN using mechanically exfoliated microflakes patterned with Cr/Au electrical contacts and supported on SiO₂/Si substrates. These on-chip devices were integrated into electrochemical microreactors^{36,45,49,50,53} with a Li–metal counter electrode and the heterostructures acting as the working electrode (Figure S1). These electrodes were immersed in a liquid

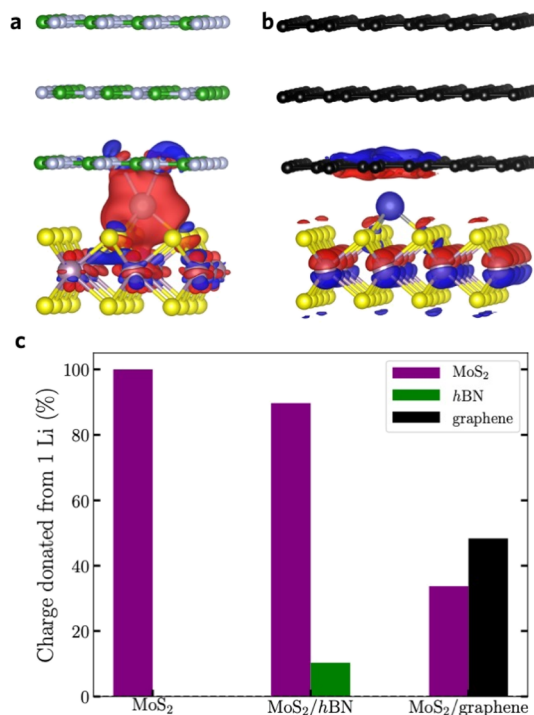


Figure 1. | Bader charge analysis of MoS₂ heterostructures. (a,b) Change in the charge density shown by isosurfaces containing 9% of the maximum charge density with the positive isosurfaces shown in red and the negative isosurfaces shown in blue when Li is introduced in the gap between hBN and MoS₂ (a), and the gap between graphene and MoS₂ (b). (c) Bader charge analysis showing the percentage of charge donated by the Li to MoS₂ (purple) as well as hBN (green) and graphene (black) in the case of freestanding MoS₂ (MoS₂), the hBN–MoS₂ heterointerface (MoS₂/hBN), and the graphene–MoS₂ heterointerface (MoS₂/graphene).

electrolyte (LiPF₆ in EC/DEC) and sealed in an airtight cell fitted with a glass window to allow for *in situ* optical and Raman characterization during intercalation. Intercalation was controlled potentiostatically by sweeping the V_{EC} between the working electrode and lithium metal. As V_{EC} was sequentially lowered from OCV (~2.5 V vs Li/Li⁺) to 0.2 V versus Li/Li⁺ at a decrement of 0.2 V, Li⁺ ions diffused through the electrolyte and intercalated into the interlayer gaps of the heterostructures. At each potential, V_{EC} was held constant to acquire Raman spectra and optical micrographs *in situ*.

To investigate the effect of a heterointerface between MoS₂ and graphene, we partially covered a MoS₂ flake with graphene to create bare and graphene-covered regions of MoS₂ (Figure 2a,b). V_{EC} was lowered from OCV to 1.0 V versus Li/Li⁺, which is the potential at which the 2H–1T' phase transition is expected to occur for bare MoS₂.^{45,49,50} In *in situ* optical microscopy revealed that the uncovered portion of MoS₂ began to darken at 1.0 V versus Li/Li⁺ (Figure 2c), indicative of the 2H–1T' phase transition.^{49,50} After 120 min at 1.0 V versus Li/Li⁺, the bare region of MoS₂ completely darkened. Strikingly, the graphene-covered region retained its original blue color even after 120 min at 1.0 V versus Li/Li⁺ (Figure 2c), suggesting that the graphene-covered MoS₂ remained in the 2H phase. The disappearance of the E_{2g} and A_{1g} modes of 2H–MoS₂ coupled with the appearance and growth of the J₁ and J₂ modes of 1T'-MoS₂^{23,55} as observed by *in situ* Raman spectroscopy confirms that the uncovered region of the MoS₂ flake underwent a phase transition at 1.0 V versus Li/Li⁺.

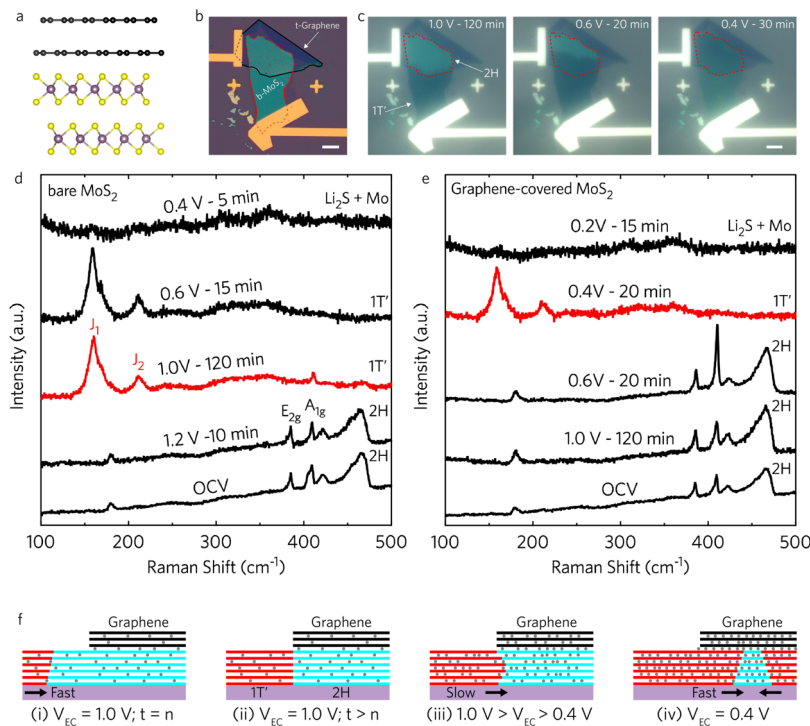


Figure 2. Heterointerface-controlled nucleation of the 1T' phase in lithiated MoS₂. (a) Schematic cross section of the atomic structure of the graphene–MoS₂ heterointerface. Mo, S, and C atoms are colored purple, yellow, and black, respectively. (b) Optical micrograph of a MoS₂ flake (red outline) partially covered by a graphene flake (black outline) with gold electrical contacts; scale bar, 10 μ m. (c) In situ optical micrographs of the heterostructure in (b) during lithium intercalation at various potentials; scale bar, 10 μ m. The dashed red line outlines graphene-covered MoS₂. The dark color of the bare MoS₂ at 1.0 V versus Li/Li⁺ is attributed to the 1T' phase, while the graphene-covered region does not completely darken until 0.4 V versus Li/Li⁺. (d) In situ Raman spectra from the center of the bare region of the MoS₂ flake in the heterostructure in (b) taken during intercalation. The 2H–1T' phase transition (red) is observed at 1.0 V versus Li/Li⁺, while the conversion reaction is observed at 0.4 V versus Li/Li⁺. (e) In situ Raman spectra from the center of the graphene-covered region of the MoS₂ flake in the heterostructure in (b) taken during intercalation. The 2H–1T' phase transition (red) is observed at 0.4 V versus Li/Li⁺, while the conversion reaction is observed at 0.2 V versus Li/Li⁺. (f) Schematic cross section of the heterogeneous nucleation of 1T'-MoS₂ (red) out of 2H-MoS₂ (blue) with arrows indicating the growth direction of the 1T' phase as a function of time (i,ii) and V_{EC} (iii,iv).

(Figure 2d). By contrast, in situ Raman spectra confirm that the graphene-covered region remained in the 2H phase after 120 min at 1.0 V versus Li/Li⁺ (Figure 2e). As V_{EC} was further lowered to 0.9, 0.8, and 0.6 V versus Li/Li⁺, the darkened region expanded inward from the bare region to the graphene-covered region of MoS₂. However, the growth of the darkened region was slow, and after 20 min at 0.6 V versus Li/Li⁺, only half of the graphene-covered region had undergone the phase transition. At 0.4 V versus Li/Li⁺, the graphene-covered MoS₂ completed the phase transition to 1T', while the bare region of MoS₂ was fully converted into Mo and Li₂S.^{49,56} For the graphene-covered region, the irreversible conversion reaction occurred at 0.2 V versus Li/Li⁺. Thus, Figure 2 shows that the graphene–MoS₂ heterointerface significantly delayed the phase transition.

Analysis of in situ optical micrographs elucidates the heterointerface effects on the growth dynamics of the 1T' domain (Figure S3). At 1.0 V versus Li/Li⁺, the bare region of MoS₂ darkened quickly inward from the flake edges in contact with the electrolyte, suggesting nucleation of 1T' domains at the edges, followed by fast growth of the 1T' domains (Figure 2f-i,ii). At 0.6 V versus Li/Li⁺, the growth of the dark region in the graphene-covered portion of the flake continues slowly from the uncovered region. Thus, when 1.0 V > V_{EC} > 0.4 V versus Li/Li⁺, 1T' domains do not nucleate in the graphene-covered region, while growth of already nucleated 1T' domains

is extremely slow (Figure 2f-iii). At 0.4 V versus Li/Li⁺, the growth of the 1T' domain accelerated significantly and also proceeded from the graphene-covered edges inward (Figure 2f-iv) until the entire covered-region of MoS₂ fully converted into the 1T' phase (Figures S3 and S4). The graphene–MoS₂ heterointerface effects on the phase transition of MoS₂ were reproduced in a replicate device (Figure S5). We note that in situ Raman spectroscopy is sufficient to study these phase transitions as Raman spectra for the 2H and 1T' phases are distinct. In situ X-ray diffraction would produce too little signal for the microflakes under study, while in situ TEM is challenging with liquid electrochemistry.

From these experiments, we conclude that the 2H–1T' phase transition initiates via heterogeneous nucleation. Our ab initio calculations show that the electron doping power of lithium to MoS₂ is reduced at the graphene–MoS₂ heterointerface, suggesting that a greater applied V_{EC} , and thus a higher lithium concentration, is required to achieve the same donated electron concentration at the graphene–MoS₂ heterointerface. However, only the top-most MoS₂ layer is expected to lose electron density to graphene, leaving the doping power of lithium in the interior vdW gaps of MoS₂ unchanged. Because our flakes are thicker than five layers, the heterointerfaced layer represents less than 20% of the volume. If the nucleation of the 1T' phase was homogeneous, that is, from the interior volume of MoS₂, we would expect a mixed Raman spectrum of both

the 2H and 1T' phases; however, we do not observe the coexistence of both phases. Therefore, we conclude that the phase transition must initiate at the heterointerface between graphene and MoS₂. Furthermore, the growth of the 1T' phase must also be heterogeneous, propagating along the heterointerface, rather than through the interior of the flake. At 1.0 V versus Li/Li⁺, the graphene-covered region of MoS₂ remained in the 2H-phase while the uncovered region fully converted into the 1T' phase, forming a lateral 2H-1T' heterointerface (Figure 2f-ii). If the growth of the 1T' phase progressed homogeneously, then the 1T' phase would be expected to grow from the interior layers at 1.0 V versus Li/Li⁺ regardless of the heterointerface at the uppermost layer, which we do not observe. This observation is consistent with previous electron diffraction analysis of intercalated bulk MoS₂ using in situ TEM, which suggested that the 2H-1T' phase transition front propagated along the top and bottom free surfaces before the interior regions.⁵⁷

The nucleation barrier for the 1T' phase can thus be modulated by a heterointerface. To further investigate the heterogeneous nucleation, we fabricated a graphene/MoS₂/graphene heterostructure in which MoS₂ is completely encapsulated by top and bottom graphene flakes with two heterointerfaces (Figure 3a,b). During the intercalation of lithium into this heterostructure, in situ optical microscopy and Raman spectroscopy revealed that the MoS₂ flake remained in the 2H phase even after V_{EC} was lowered to 0.4 V versus Li/Li⁺ (Figure 3c,d), an applied voltage at which pristine MoS₂ breaks down to Mo clusters and Li₂S (Figure 2d). The 1T' phase was finally nucleated when V_{EC} was lowered to 0.2 V versus Li/Li⁺, at which point the flake darkened (Figure 3c) and the J_1 and J_2 peaks of 1T'-MoS₂ appeared (Figure 3d). The delayed phase transition might be because the MoS₂ flake was not directly exposed to the liquid electrolyte. However, in our previous study, we showed that MoS₂ still underwent the phase transition at 1.0 V versus Li/Li⁺ despite not being exposed to the electrolyte.⁴⁵ Further intercalation of this heterostructure was not possible due to the destruction of the electrical contacts from the alloying of gold with lithium at 0.2 V versus Li/Li⁺.^{58,59} Intercalation of a replicate device showed similar results (Figure S6; lithium intercalation into the graphene flakes is shown in Figure S7). Thus, using two differently configured heterostructures (Figures 2 and 3), we clearly demonstrated a delay in the phase transition of up to 0.8 V, which we attribute to the heterogeneous nucleation and heterogeneous growth of the 1T' phase.

We next investigated the growth kinetics of the 1T' phase at different heterointerfaces by intercalating a heterostructure of MoS₂ partially supported on graphene and partially on SiO₂ where the top basal plane of MoS₂ was exposed to the electrolyte to initiate the nucleation at the top-most layer (Figure 4a,b). Surprisingly, the bottom graphene-MoS₂ heterointerface accelerated the phase transition instead of delaying it. In situ optical micrographs and Raman spectra shown in Figure 4c–e reveal that the graphene-supported region of the MoS₂ flake not only underwent the phase transition at 1.0 V versus Li/Li⁺ as expected due to the free top-most layer of MoS₂, but also did so faster than the SiO₂-supported region of MoS₂. The graphene-supported region completed the phase transition after 30 min at 1.0 V versus Li/Li⁺, while the SiO₂-supported region did so after 70 min at 1.0 V versus Li/Li⁺. Both regions underwent the irreversible conversion reaction as expected at 0.4 V versus Li/Li⁺ (Figure

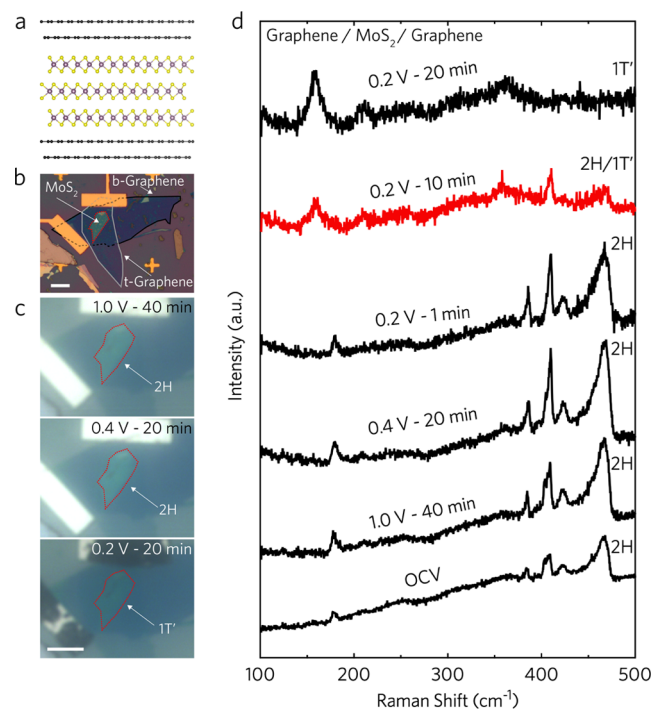


Figure 3. Graphene-encapsulation of MoS₂ significantly delays the 2H-1T' phase transition. (a) Schematic cross section of the atomic structure of a graphene/MoS₂/graphene heterostructure; Mo, S, and C atoms are colored purple, yellow, and black, respectively. In actual devices, the flakes are several layers thick. (b) Optical micrograph of a MoS₂ flake (red outline) encapsulated by top (gray outline) and bottom (black outline) graphene flakes with gold electrical contacts; scale bar, 10 μ m. (c) In situ optical micrographs of the heterostructure in (b) during lithium intercalation; scale bar, 10 μ m. The dashed red line indicates the location of the encapsulated MoS₂ flake. The MoS₂ remains unchanged until 0.2 V versus Li/Li⁺, at which point it darkens, indicating the onset of the 1T' phase; scale bar, 10 μ m. The black discoloration of the gold contacts at 0.2 V versus Li/Li⁺ indicates the alloying of gold with lithium. (d) In situ Raman spectra from the center of the MoS₂ flake in the heterostructure in (b) taken during intercalation. The flake remains in the 2H phase down to 0.4 V versus Li/Li⁺, and the onset of the 2H-1T' phase transition is observed only after intercalating at 0.2 V versus Li/Li⁺ for 10 min, with the full transition observed after 20 min.

4d,e), and we observed the same behavior in a replicate device (Figure S8). This indicates that the mere presence of a graphene–MoS₂ heterointerface is not sufficient to delay the phase transition.

To understand the faster growth kinetics at a MoS₂–graphene heterointerface at the bottom of the MoS₂ flake, we considered two possibilities. The first is more efficient electron injection into MoS₂ for faster intercalation kinetics as graphene makes superior electrical contact to MoS₂ than gold does due to a reduced Schottky barrier at the interface.^{60,61} Thus, it is possible that the graphene–MoS₂ heterointerface facilitated more efficient electron injection than the gold electrode, allowing for a more rapid phase transition to the 1T' phase. However, intercalation of a MoS₂ flake partially supported on graphene and biased only through MoS₂ showed the same enhancement in the phase transition kinetics, eliminating the possibility of enhanced charge injection (Figure S9).

The second possibility is that the graphene support could facilitate the release of mechanical strain induced by the phase transition. The 2H-1T' phase transition induces mechanical

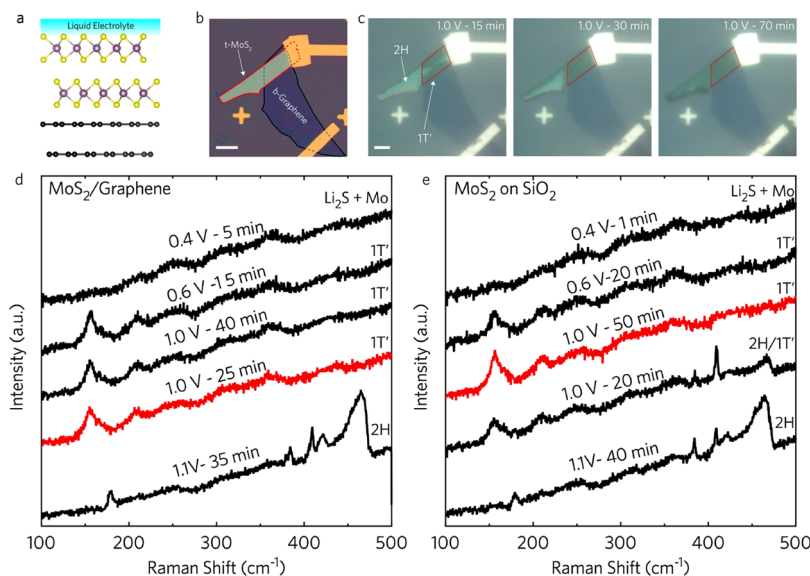


Figure 4. Kinetics of the 2H-1T' phase transition in MoS₂. (a) Schematic cross section of the atomic structure of a MoS₂/graphene heterointerface where the top basal plane of MoS₂ is in direct contact with the liquid electrolyte; Mo, S, and C atoms are colored purple, yellow, and black, respectively. In actual devices, the flakes are several layers thick. (b) Optical micrograph of a MoS₂ flake (red outline) partially supported on a graphene flake (black outline) with gold electrical contacts; scale bar, 10 μ m. (c) In situ optical micrographs of the heterostructure in (b) during lithium intercalation at various potentials; scale bar, 10 μ m. The region of the MoS₂ flake supported on graphene is outlined in red. The dark color of MoS₂ at 1.0 V versus Li/Li⁺ is attributed to the 1T' phase, and the graphene-supported region of MoS₂ completes the phase transition faster than the SiO₂-supported region of MoS₂. (d) In situ Raman spectra from the center of the graphene-supported region of the MoS₂ flake in the heterostructure in (b) taken during intercalation. The 2H-1T' phase transition (red) is observed after 25 min at 1.0 V versus Li/Li⁺, while the conversion reaction is observed at 0.4 V versus Li/Li⁺. (e) In situ Raman spectra from the center of the SiO₂-supported region of the MoS₂ flake in the heterostructure in (b) taken during intercalation. The 2H-1T' phase transition (red) is observed after 50 min at 1.0 V versus Li/Li⁺, while the conversion reaction is observed at 0.4 V versus Li/Li⁺.

strain, which can result in the formation of wrinkles and a buckled microstructure.⁵⁰ Post mortem SEM of the MoS₂-graphene heterostructures after intercalation revealed the formation of wrinkles and a buckled microstructure in the MoS₂ flakes after the phase transition (Figure S10). We confirmed that this wrinkled microstructure formed as a result of the phase transition and not due to high levels of intercalated lithium (Figure S11). Our key observation from the post mortem SEM analysis was that the height and density of the wrinkles and buckling was significantly enhanced in the region of the MoS₂ flakes supported on graphene as compared to the regions of MoS₂ supported on SiO₂. This enhancement suggests that the mechanical strain developed during the phase transition was more easily released via the formation of wrinkles in MoS₂ supported on graphene than on amorphous SiO₂. We therefore attribute the increased phase transition kinetics in graphene-supported MoS₂ to the more efficient release of strain between MoS₂ and graphene during the phase transition.

We next examined if the effects of a heterointerface on the thermodynamics and kinetics of the phase transition in MoS₂ were specific to graphene or occurred simply due to the presence of a 2D heterointerface. Our ab initio calculations suggest that while the graphene-MoS₂ heterointerface will reduce lithium's electron doping power to MoS₂, an hBN-MoS₂ interface should have little effect on the doping power of lithium. To probe this, we fabricated a heterostructure where MoS₂ was partially covered by hBN (Figure 5a,b) and observed that the hBN-covered MoS₂ underwent the phase transition at 1.0 V versus Li/Li⁺ (Figures 5c,d and S12a), in agreement with our calculations and our previous findings.⁴⁵ Therefore, we conclude that the identity of the top heterointerface with MoS₂

and the resulting distribution of donated electron density at that heterointerface are key to determine the thermodynamics of the phase transition.

We also probed the kinetics of the phase transition at the heterointerface by fabricating a heterostructure where MoS₂ was partially supported on hBN and partially on SiO₂, with the free top basal plane of MoS₂ exposed to the electrolyte (Figure 5e,f). Similar to the graphene-supported case, the hBN-supported MoS₂ underwent the phase transition more rapidly at 1.0 V versus Li/Li⁺ than the SiO₂-supported region (Figures 5g,h and S12b). Post mortem SEM of this heterostructure revealed a more pronounced wrinkled microstructure of the hBN-supported region as compared to the SiO₂-supported region (Figure S12c–e). This suggests that unlike the thermodynamic control achievable with the top heterointerface, the kinetic control of a bottom heterointerface is not specific to the identity of the 2D support. We conclude that the origin of the enhanced kinetics on a 2D support as compared to on amorphous SiO₂ is likely due to the weak vdW interactions between layers that facilitate the rapid formation of a wrinkled microstructure. This is supported by the exfoliation mechanism of few-layer 2D flakes from bulk crystals onto amorphous SiO₂ using scotch tape or an AFM-tip.⁶² In both cases, the interaction of 2D flakes with SiO₂ is stronger than their interlayer coupling, allowing for a few layers to remain stuck to the substrate. Thus, we show that the weaker vdW interactions between MoS₂ and a 2D support as compared to the MoS₂-SiO₂ interface allow for the more efficient release of mechanical strain and enhance the kinetics of the phase transition.

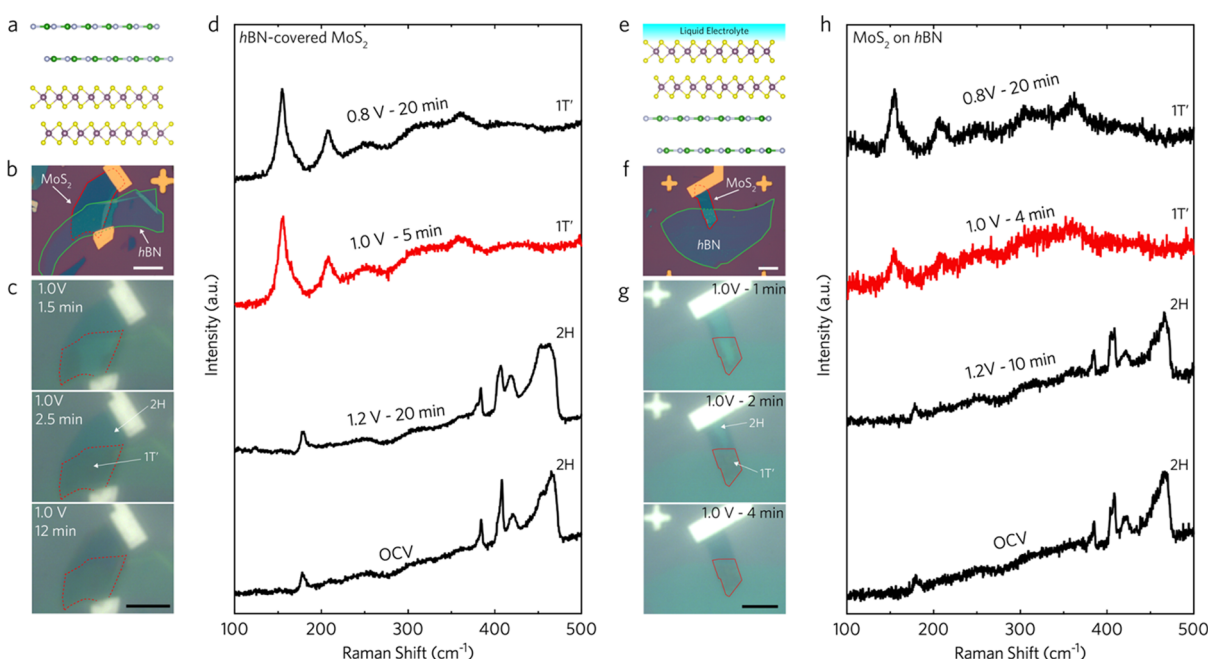


Figure 5. Phase dynamics in lithiated MoS_2/hBN heterostructures. (a) Schematic cross section of the atomic structure of the hBN/MoS_2 heterointerface with Mo, S, N, and B atoms colored purple, yellow, white, and green, respectively. (b) Optical micrograph of MoS_2 (red) partially covered by hBN (green) with gold contacts; scale bar, $10 \mu\text{m}$. (c) In situ optical micrographs of the heterostructure in (b) during lithium intercalation; scale bar, $10 \mu\text{m}$. The dashed red line outlines hBN -covered MoS_2 . The darkening of MoS_2 is attributed to the $1\text{T}'$ phase. (d) In situ Raman spectra from the center of the hBN -covered region of MoS_2 in the heterostructure in (b) during intercalation. The $1\text{T}'$ phase (red) appears at 1.0 V versus Li/Li^+ . (e) Schematic cross section of the atomic structure of a MoS_2/hBN heterointerface where the top basal plane of MoS_2 is in direct contact with the liquid electrolyte; Mo, S, N, and B atoms are colored purple, yellow, white, and green, respectively. In actual devices, the flakes are several-layers thick. (f) Optical micrograph of MoS_2 (red) partially supported on hBN (green) with gold contacts; scale bar, $10 \mu\text{m}$. (g) In situ optical micrographs of the heterostructure in (f) during lithium intercalation; scale bar, $10 \mu\text{m}$. The red line outlines hBN -supported MoS_2 . The darkening of MoS_2 is attributed to the $1\text{T}'$ phase. (h) In situ Raman spectra from the center of the hBN -supported region of MoS_2 in the heterostructure in (f) during intercalation. The $1\text{T}'$ phase (red) appears at 1.0 V versus Li/Li^+ .

CONCLUSIONS

In summary, our results provide the first experimental evidence that the kinetics and thermodynamics of the lithium-induced phase transition in MoS_2 nanosheets can be modified by heterointerfaces, and consequently, we discovered that the nucleation of the $1\text{T}'$ phase is a heterogeneous nucleation process. We show that the nucleation barrier for the $1\text{T}'$ phase is the highest for the graphene– MoS_2 interface, requiring an increase in V_{EC} as high as 0.8 V more than for the free MoS_2 surface. The growth kinetics of the phase transition are also influenced by the heterointerface, where 2D vdW interfaces facilitate faster growth kinetics than MoS_2 supported on SiO_2 . Our results thus provide microscopic insights into the nucleation pathways for phase transitions in 2D nanomaterials and highlight the importance of heterointerfaces on the onset and propagation of phase transitions. Particularly, as graphene and hBN are widely employed as nanoscaled electrodes and passivation layers for many 2D heterostructures, understanding their heterointerfacial effects on phase transition dynamics of the active material is of paramount importance. These insights can be applied to the engineering of nanoscaled energy storage and conversion technologies that utilize heterostructures to further optimize their performance.

ASSOCIATED CONTENT

Supporting Information

The Supporting Information is available free of charge at <https://pubs.acs.org/doi/10.1021/acsanm.1c03402>.

Raman characterization of 2D crystals, density of states for intercalated $\text{MoS}_2/\text{graphene}$, additional in situ optical images supporting Figure 2, analysis of optical images for Figure 2, in situ data for a replicate graphene/ MoS_2 heterostructure, in situ data for a replicate graphene/ $\text{MoS}_2/\text{graphene}$ heterostructure, in situ Raman spectra of intercalated graphene, in situ data for a replicate $\text{MoS}_2/\text{graphene}$ heterostructure, in situ data for a $\text{MoS}_2/\text{graphene}$ heterostructure biased only through MoS_2 , post mortem analysis of $\text{MoS}_2/\text{graphene}$ heterostructures, intercalation of bare MoS_2 , and additional in situ data and post mortem analysis for Figure 5 (PDF)

AUTHOR INFORMATION

Corresponding Author

Judy J. Cha – Department of Mechanical Engineering and Materials Science, Yale University, New Haven, Connecticut 06511, United States; Energy Sciences Institute, West Haven, Connecticut 06516, United States; orcid.org/0000-0002-6346-2814; Email: judy.cha@yale.edu

Authors

Joshua V. Pondick – Department of Mechanical Engineering and Materials Science, Yale University, New Haven, Connecticut 06511, United States; Energy Sciences Institute, West Haven, Connecticut 06516, United States; orcid.org/0003-3380-2686

Aakash Kumar — *Department of Mechanical Engineering and Materials Science, Yale University, New Haven, Connecticut 06511, United States; Energy Sciences Institute, West Haven, Connecticut 06516, United States*

Mengjing Wang — *Department of Mechanical Engineering and Materials Science, Yale University, New Haven, Connecticut 06511, United States; Energy Sciences Institute, West Haven, Connecticut 06516, United States;  orcid.org/0000-0003-1195-4515*

Sajad Yazdani — *Department of Mechanical Engineering and Materials Science, Yale University, New Haven, Connecticut 06511, United States; Energy Sciences Institute, West Haven, Connecticut 06516, United States*

John M. Woods — *Department of Mechanical Engineering and Materials Science, Yale University, New Haven, Connecticut 06511, United States; Energy Sciences Institute, West Haven, Connecticut 06516, United States*

Diana Y. Qiu — *Department of Mechanical Engineering and Materials Science, Yale University, New Haven, Connecticut 06511, United States; Energy Sciences Institute, West Haven, Connecticut 06516, United States*

Complete contact information is available at:
<https://pubs.acs.org/10.1021/acsanm.1c03402>

Author Contributions

J.V.P. and J.J.C. conceived the project. J.V.P. carried out the experiments with assistance from M.W. Ab initio calculations were performed by A.K. and D.Y.Q. S.Y. and J.M.W. contributed to the development of experimental methods and characterization techniques. J.V.P. and J.J.C. wrote the manuscript with input from all authors.

Notes

The authors declare no competing financial interest.

ACKNOWLEDGMENTS

J.V.P. was supported by the National Defense Science and Engineering Graduate (NDSEG) Fellowship Program, sponsored by the Air Force Research Laboratory (AFRL), the Office of Naval Research (ONR), and the Army Research Office (ARO). J.J.C. acknowledges support from the National Science Foundation (CAREER #1749742). Device fabrication and characterization were carried out at the Yale West Campus Materials Characterization Core and the Yale West Campus Cleanroom. D.Y.Q. and A.K. acknowledge support from the National Science Foundation under grant no. DMR 2114081. The calculations used resources of the National Energy Research Scientific Computing Center (NERSC), a DOE Office of Science User Facility supported by the Office of Science of the U.S. Department of Energy under contract no. DE-AC02-05CH11231 and the Extreme Science and Engineering Discovery Environment (XSEDE), which is supported by the Office of Science of the U.S. Department of Energy under contract no. DE-AC05-00OR22725. We also thank the Yale Center for Research Computing, specifically the Grace cluster for the computing resources.

REFERENCES

- (1) Sleutel, M.; Van Den Broeck, I.; Van Gerven, N.; Feuillie, C.; Jonckheere, W.; Valotteau, C.; Dufrêne, Y. F.; Remaut, H. Nucleation and Growth of a Bacterial Functional Amyloid at Single-Fiber Resolution. *Nat. Chem. Biol.* **2017**, *13*, 902–908.
- (2) Van Driessche, A. E. S.; Van Gerven, N.; Bomans, P. H. H.; Joosten, R. R. M.; Friedrich, H.; Gil-Carton, D.; Sommerdijk, N. A. J.; Sleutel, M. Molecular Nucleation Mechanisms and Control Strategies for Crystal Polymorph Selection. *Nature* **2018**, *556*, 89–94.
- (3) Schmidt-Cernohorska, M.; Zhernov, I.; Steib, E.; Le Guenec, M.; Achek, R.; Borgers, S.; Demurtas, D.; Mouawad, L.; Lansky, Z.; Hamel, V.; Guichard, P. Flagellar Microtubule Doublet Assembly In Vitro Reveals a Regulatory Role of Tubulin C-Terminal Tails. *Science* **2019**, *363*, 285–288.
- (4) Daneshvar, K.; Ardehali, M. B.; Klein, I. A.; Hsieh, F.-K.; Kratkiewicz, A. J.; Mahpour, A.; Cancelliere, S. O. L.; Zhou, C.; Cook, B. M.; Li, W.; Pondick, J. V.; Gupta, S. K.; Moran, S. P.; Young, R. A.; Kingston, R. E.; Mullen, A. C. LncRNA DIGIT and BRD3 Protein Form Phase-Separated Condensates to Regulate Endoderm Differentiation. *Nat. Cell Biol.* **2020**, *22*, 1211–1222.
- (5) Kirkby, J.; Duplissy, J.; Sengupta, K.; Frege, C.; Gordon, H.; Williamson, C.; Heinritzi, M.; Simon, M.; Yan, C.; Almeida, J.; Tröstl, J.; Nieminen, T.; Ortega, I. K.; Wagner, R.; Adamov, A.; Amorim, A.; Bernhammer, A.-K.; Bianchi, F.; Breitenlechner, M.; Brilke, S.; et al. Ion-Induced Nucleation of Pure Biogenic Particles. *Nature* **2016**, *533*, 521–526.
- (6) Kiselev, A.; Bachmann, F.; Pedevilla, P.; Cox, S. J.; Michaelides, A.; Gerthsen, D.; Leisner, T. Active Sites in Heterogeneous Ice Nucleation—the Example of K-Rich Feldspars. *Science* **2017**, *355*, 367–371.
- (7) Zou, L.; Yang, C.; Lei, Y.; Zakharov, D.; Wierzorek, J. M. K.; Su, D.; Yin, Q.; Li, J.; Liu, Z.; Stach, E. A.; Yang, J. C.; Qi, L.; Wang, G.; Zhou, G. Dislocation Nucleation Facilitated by Atomic Segregation. *Nat. Mater.* **2018**, *17*, 56–63.
- (8) Zhou, J.; Yang, Y.; Yang, Y.; Kim, D. S.; Yuan, A.; Tian, X.; Ophus, C.; Sun, F.; Schmid, A. K.; Nathanson, M.; Heinz, H.; An, Q.; Zeng, H.; Ercius, P.; Miao, J. Observing Crystal Nucleation in Four Dimensions Using Atomic Electron Tomography. *Nature* **2019**, *570*, 500–503.
- (9) Jeon, S.; Heo, T.; Hwang, S.-Y.; Ciston, J.; Bustillo, K. C.; Reed, B. W.; Ham, J.; Kang, S.; Kim, S.; Lim, J.; Lim, K.; Kim, J. S.; Kang, M.-H.; Bloom, R. S.; Hong, S.; Kim, K.; Zettl, A.; Kim, W. Y.; Ercius, P.; Park, J.; Lee, W. C. Reversible Disorder-Order Transitions in Atomic Crystal Nucleation. *Science* **2021**, *371*, 498–503.
- (10) Loh, N. D.; Sen, S.; Bosman, M.; Tan, S. F.; Zhong, J.; Nijhuis, C. A.; Král, P.; Matsudaira, P.; Mirsaidov, U. Multistep Nucleation of Nanocrystals in Aqueous Solution. *Nat. Chem.* **2017**, *9*, 77–82.
- (11) Liu, J.; Shi, W.; Ni, B.; Yang, Y.; Li, S.; Zhuang, J.; Wang, X. Incorporation of Clusters within Inorganic Materials through Their Addition during Nucleation Steps. *Nat. Chem.* **2019**, *11*, 839–845.
- (12) Cao, K.; Biskupek, J.; Stroppiello, C. T.; McSweeney, R. L.; Chamberlain, T. W.; Liu, Z.; Suenaga, K.; Skowron, S. T.; Besley, E.; Khlobystov, A. N.; Kaiser, U. Atomic Mechanism of Metal Crystal Nucleus Formation in a Single-Walled Carbon Nanotube. *Nat. Chem.* **2020**, *12*, 921–928.
- (13) De Yoreo, J. J.; Gilbert, P. U.; Sommerdijk, N. A.; Penn, R. L.; Whitelam, S.; Joester, D.; Zhang, H.; Rimer, J. D.; Navrotsky, A.; Banfield, J. F.; Wallace, A. F.; Michel, F. M.; Meldrum, F. C.; Cölfen, H.; Dove, P. M. Crystallization by Particle Attachment in Synthetic, Biogenic, and Geologic Environments. *Science* **2015**, *349*, aaa6760.
- (14) Yang, H.; Kim, S. W.; Chhowalla, M.; Lee, Y. H. Structural and Quantum-State Phase Transition in van der Waals Layered Materials. *Nat. Phys.* **2017**, *13*, 931–937.
- (15) Yoshida, M.; Suzuki, R.; Zhang, Y.; Nakano, M.; Iwasa, Y. Memristive Phase Switching in Two-Dimensional 1T-TaS₂ Crystals. *Sci. Adv.* **2015**, *1*, No. e1500606.
- (16) Zhang, F.; Zhang, H.; Krylyuk, S.; Milligan, C. A.; Zhu, Y.; Zemlyanov, D. Y.; Bendersky, L. A.; Burton, B. P.; Davydov, A. V.; Appenzeller, J. Electric-Field Induced Structural Transition in Vertical MoTe₂- and Mo_{1-x}W_xTe₂-Based Resistive Memories. *Nat. Mater.* **2019**, *18*, 55–61.
- (17) Zhu, X.; Li, D.; Liang, X.; Lu, W. D. Ionic Modulation and Ionic Coupling Effects in MoS₂ Devices for Neuromorphic Computing. *Nat. Mater.* **2019**, *18*, 141–148.
- (18) Voiry, D.; Yamaguchi, H.; Li, J.; Silva, R.; Alves, D. C. B.; Fujita, T.; Chen, M.; Asefa, T.; Shenoy, V. B.; Eda, G.; Chhowalla, M.

Enhanced Catalytic Activity in Strained Chemically Exfoliated WS₂ Nanosheets for Hydrogen Evolution. *Nat. Mater.* **2013**, *12*, 850–855.

(19) Lukowski, M. A.; Daniel, A. S.; Meng, F.; Forticaux, A.; Li, L.; Jin, S. Enhanced Hydrogen Evolution Catalysis from Chemically Exfoliated Metallic MoS₂ Nanosheets. *J. Am. Chem. Soc.* **2013**, *135*, 10274–10277.

(20) Wang, H.; Lu, Z.; Xu, S.; Kong, D.; Cha, J. J.; Zheng, G.; Hsu, P.-C.; Yan, K.; Bradshaw, D.; Prinz, F. B.; Cui, Y. Electrochemical Tuning of Vertically Aligned MoS₂ Nanofilms and Its Application in Improving Hydrogen Evolution Reaction. *Proc. Natl. Acad. Sci. U.S.A.* **2013**, *110*, 19701–19706.

(21) Voiry, D.; Fullon, R.; Yang, J.; de Carvalho Castro e Silva, C.; Kappera, R.; Bozkurt, I.; Kaplan, D.; Lagos, M. J.; Batson, P. E.; Gupta, G.; Mohite, A. D.; Dong, L.; Er, D.; Shenoy, V. B.; Asefa, T.; Chhowalla, M. The Role of Electronic Coupling Between Substrate and 2D MoS₂ Nanosheets in Electrocatalytic Production of Hydrogen. *Nat. Mater.* **2016**, *15*, 1003.

(22) Yazdani, S.; Yarali, M.; Cha, J. J. Recent Progress on In Situ Characterizations of Electrochemically Intercalated Transition Metal Dichalcogenides. *Nano Res.* **2019**, *12*, 2126–2139.

(23) Kappera, R.; Voiry, D.; Yalcin, S. E.; Branch, B.; Gupta, G.; Mohite, A. D.; Chhowalla, M. Phase-Engineered Low-Resistance Contacts for Ultrathin MoS₂ Transistors. *Nat. Mater.* **2014**, *13*, 1128–1134.

(24) Leng, K.; Chen, Z.; Zhao, X.; Tang, W.; Tian, B.; Nai, C. T.; Zhou, W.; Loh, K. P. Phase Restructuring in Transition Metal Dichalcogenides for Highly Stable Energy Storage. *ACS Nano* **2016**, *10*, 9208–9215.

(25) Zhang, L.; Sun, D.; Kang, J.; Feng, J.; Bechtel, H. A.; Wang, L.-W.; Cairns, E. J.; Guo, J. Electrochemical Reaction Mechanism of the MoS₂ Electrode in a Lithium-Ion Cell Revealed by In Situ and Operando X-Ray Absorption Spectroscopy. *Nano Lett.* **2018**, *18*, 1466–1475.

(26) Quilty, C. D.; Housel, L. M.; Bock, D. C.; Dunkin, M. R.; Wang, L.; Lutz, D. M.; Abraham, A.; Bruck, A. M.; Takeuchi, E. S.; Takeuchi, K. J.; Marschilok, A. C. Ex Situ and Operando XRD and XAS Analysis of MoS₂: A Lithiation Study of Bulk and Nanosheet Materials. *ACS Appl. Energy Mater.* **2019**, *2*, 7635–7646.

(27) Chen, B.; Chao, D.; Liu, E.; Jaroniec, M.; Zhao, N.; Qiao, S.-Z. Transition Metal Dichalcogenides for Alkali Metal Ion Batteries: Engineering Strategies at the Atomic Level. *Energy Environ. Sci.* **2020**, *13*, 1096–1131.

(28) Kertesz, M.; Hoffmann, R. Octahedral vs. Trigonal-Prismatic Coordination and Clustering in Transition-Metal Dichalcogenides. *J. Am. Chem. Soc.* **1984**, *106*, 3453–3460.

(29) Dungey, K. E.; Curtis, M. D.; Penner-Hahn, J. E. Structural Characterization and Thermal Stability of MoS₂ Intercalation Compounds. *Chem. Mater.* **1998**, *10*, 2152–2161.

(30) Wang, L.; Xu, Z.; Wang, W.; Bai, X. Atomic Mechanism of Dynamic Electrochemical Lithiation Processes of MoS₂ Nanosheets. *J. Am. Chem. Soc.* **2014**, *136*, 6693–6697.

(31) Wang, C.; He, Q.; Halim, U.; Liu, Y.; Zhu, E.; Lin, Z.; Xiao, H.; Duan, X.; Feng, Z.; Cheng, R.; Weiss, N. O.; Ye, G.; Huang, Y.-C.; Wu, H.; Cheng, H.-C.; Shakir, I.; Liao, L.; Chen, X.; Goddard III, W. A.; Huang, Y.; Duan, X. Monolayer Atomic Crystal Molecular Superlattices. *Nature* **2018**, *555*, 231–236.

(32) *Intercalation in Layered Materials*; Dresselhaus, M. S., Ed.; Springer Science+Business Media LLC: New York, 1986.

(33) Eda, G.; Yamaguchi, H.; Voiry, D.; Fujita, T.; Chen, M.; Chhowalla, M. Photoluminescence from Chemically Exfoliated MoS₂. *Nano Lett.* **2011**, *11*, 5111–5116.

(34) Chhowalla, M.; Shin, H. S.; Eda, G.; Li, L.-J.; Loh, K. P.; Zhang, H. The Chemistry of Two-Dimensional Layered Transition Metal Dichalcogenide Nanosheets. *Nat. Chem.* **2013**, *5*, 263–275.

(35) Wan, J.; Lacey, S. D.; Dai, J.; Bao, W.; Fuhrer, M. S.; Hu, L. Tuning Two-Dimensional Nanomaterials by Intercalation: Materials, Properties and Applications. *Chem. Soc. Rev.* **2016**, *45*, 6742–6765.

(36) Bediako, D. K.; Rezaee, M.; Yoo, H.; Larson, D. T.; Zhao, S. Y. F.; Taniguchi, T.; Watanabe, K.; Brower-Thomas, T. L.; Kaxiras, E.; Kim, P. Heterointerface Effects in the Electrointercalation of van der Waals Heterostructures. *Nature* **2018**, *558*, 425–429.

(37) Blöchl, P. E. Projector Augmented-Wave Method. *Phys. Rev. B: Condens. Matter Mater. Phys.* **1994**, *50*, 17953–17979.

(38) Dal Corso, A. Pseudopotentials Periodic Table: From H to Pu. *Comput. Mater. Sci.* **2014**, *95*, 337–350.

(39) Giannozzi, P.; Baroni, S.; Bonini, N.; Calandra, M.; Car, R.; Cavazzoni, C.; Ceresoli, D.; Chiarotti, G. L.; Cococcioni, M.; Dabo, I.; Dal Corso, A.; de Gironcoli, S.; Fabris, S.; Fratesi, G.; Gebauer, R.; Gerstmann, U.; Gougoussis, C.; Kokalj, A.; Lazzeri, M.; Martin-Samos, L.; et al. QUANTUM ESPRESSO: A Modular and Open-Source Software Project for Quantum Simulations of Materials. *J. Phys. Condens. Matter* **2009**, *21*, 395502.

(40) Perdew, J. P.; Burke, K.; Ernzerhof, M. Generalized Gradient Approximation Made Simple. *Phys. Rev. Lett.* **1996**, *78*, 1396.

(41) Grimme, S.; Antony, J.; Ehrlich, S.; Krieg, H. A Consistent and Accurate Ab Initio Parametrization of Density Functional Dispersion Correction (DFT-D) for the 94 Elements H–Pu. *J. Chem. Phys.* **2010**, *132*, 154104.

(42) Monkhorst, H. J.; Pack, J. D. Special Points for Brillouin-Zone Integrations. *Phys. Rev. B: Condens. Matter Mater. Phys.* **1976**, *13*, 5188–5192.

(43) Larson, D. T.; Fampiou, I.; Kim, G.; Kaxiras, E. Lithium Intercalation in Graphene-MoS₂ Heterostructures. *J. Phys. Chem. C* **2018**, *122*, 24535–24541.

(44) Tang, W.; Sanville, E.; Henkelman, G. A Grid-Based Bader Analysis Algorithm without Lattice Bias. *J. Phys. Condens. Matter* **2009**, *21*, 084204.

(45) Yazdani, S.; Pondick, J. V.; Kumar, A.; Yarali, M.; Woods, J. M.; Hynek, D. J.; Qiu, D. Y.; Cha, J. J. Heterointerface Effects on Lithium-Induced Phase Transitions in Intercalated MoS₂. *ACS Appl. Mater. Interfaces* **2021**, *13*, 10603–10611.

(46) Li, S.-L.; Miyazaki, H.; Song, H.; Kuramochi, H.; Nakahara, S.; Tsukagoshi, K. Quantitative Raman Spectrum and Reliable Thickness Identification for Atomic Layers on Insulating Substrates. *ACS Nano* **2012**, *6*, 7381–7388.

(47) Lee, C.; Yan, H.; Brus, L. E.; Heinz, T. F.; Hone, J.; Ryu, S. Anomalous Lattice Vibrations of Single-and Few-Layer MoS₂. *ACS Nano* **2010**, *4*, 2695–2700.

(48) Pondick, J. V.; Yazdani, S.; Yarali, M.; Reed, S. N.; Hynek, D. J.; Cha, J. J. The Effect of Mechanical Strain on Lithium Staging in Graphene. *Adv. Electron. Mater.* **2021**, *7*, 2000981.

(49) Wan, J.; Bao, W.; Liu, Y.; Dai, J.; Shen, F.; Zhou, L.; Cai, X.; Urban, D.; Li, Y.; Jungi Johann, K.; Fuhrer, M. S.; Hu, L. In Situ Investigations of Li-MoS₂ with Planar Batteries. *Adv. Energy Mater.* **2015**, *5*, 1401742.

(50) Xiong, F.; Wang, H.; Liu, X.; Sun, J.; Brongersma, M.; Pop, E.; Cui, Y. Li Intercalation in MoS₂: In Situ Observation of Its Dynamics and Tuning Optical and Electrical Properties. *Nano Lett.* **2015**, *15*, 6777–6784.

(51) Zhang, J.; Yang, A.; Wu, X.; van de Groep, J.; Tang, P.; Li, S.; Liu, B.; Shi, F.; Wan, J.; Li, Q.; Sun, Y.; Lu, Z.; Zheng, X.; Zhou, G.; Wu, C.-L.; Zhang, S.-C.; Brongersma, M. L.; Li, J.; Cui, Y. Reversible and Selective Ion Intercalation through the Top Surface of Few-Layer MoS₂. *Nat. Commun.* **2018**, *9*, 5289.

(52) *Graphite Intercalation Compounds I*; Zabel, H.; Solin, S. A., Eds.; Springer-Verlag: New York, 1990.

(53) Kühne, M.; Paolucci, F.; Popovic, J.; Ostrovsky, P. M.; Maier, J.; Smet, J. H. Ultrafast Lithium Diffusion in Bilayer Graphene. *Nat. Nanotechnol.* **2017**, *12*, 895–900.

(54) Zhao, S. Y. F.; Elbaz, G. A.; Bediako, D. K.; Yu, C.; Efetov, D. K.; Guo, Y.; Ravichandran, J.; Min, K.-A.; Hong, S.; Taniguchi, T.; Watanabe, K.; Brus, L. E.; Roy, X.; Kim, P. Controlled Electrochemical Intercalation of Graphene/h-BN van der Waals Heterostructures. *Nano Lett.* **2018**, *18*, 460–466.

(55) Jiménez Sandoval, S.; Yang, D.; Frindt, R. F.; Irwin, J. C. Raman Study and Lattice Dynamics of Single Molecular Layers of MoS₂. *Phys. Rev. B: Condens. Matter Mater. Phys.* **1991**, *44*, 3955–3962.

(56) Xiao, J.; Choi, D.; Cosimbescu, L.; Koech, P.; Liu, J.; Lemmon, J. P. Exfoliated MoS₂ Nanocomposite as an Anode Material for Lithium Ion Batteries. *Chem. Mater.* **2010**, *22*, 4522–4524.

(57) Chen, S.; Wang, L.; Shao, R.; Zou, J.; Cai, R.; Lin, J.; Zhu, C.; Zhang, J.; Xu, F.; Cao, J.; Feng, J.; Qi, J.; Gao, P.; Qi, J.; Gao, P. Atomic Structure and Migration Dynamics of MoS₂/Li_xMoS₂ Interface. *Nano Energy* **2018**, *48*, 560–568.

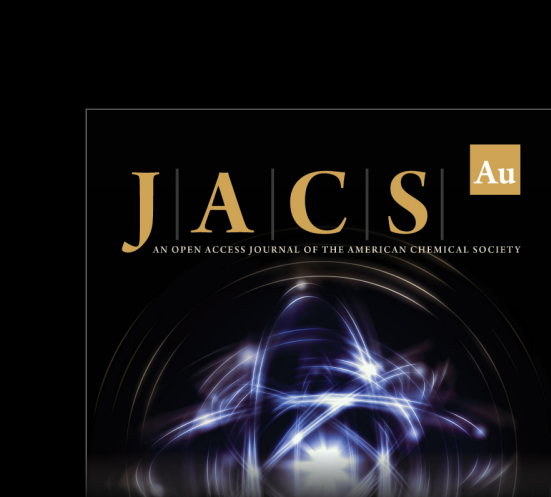
(58) Taillades, G.; Benjelloun, N.; Sarradin, J.; Ribes, M. Metal-Based Very Thin Film Anodes for Lithium Ion Microbatteries. *Solid State Ionics* **2002**, *152-153*, 119–124.

(59) Zeng, Z.; Liang, W.-I.; Chu, Y.-H.; Zheng, H. In Situ TEM Study of the Li-Au Reaction in an Electrochemical Liquid Cell. *Faraday Discuss.* **2014**, *176*, 95–107.

(60) Zhou, Y.; Silva, J. L.; Woods, J. M.; Pondick, J. V.; Feng, Q.; Liang, Z.; Liu, W.; Lin, L.; Deng, B.; Brenna, B.; Xia, F.; Peng, H.; Liu, Z.; Wang, H.; Araujo, C. M.; Cha, J. J. Revealing the Contribution of Individual Factors to Hydrogen Evolution Reaction Catalytic Activity. *Adv. Mater.* **2018**, *30*, 1706076.

(61) Zhou, Y.; Pondick, J. V.; Silva, J. L.; Woods, J. M.; Hynek, D. J.; Matthews, G.; Shen, X.; Feng, Q.; Liu, W.; Lu, Z.; Liang, Z.; Brenna, B.; Cai, Z.; Wu, M.; Jiao, L.; Hu, S.; Wang, H.; Araujo, C. M.; Cha, J. J. Unveiling the Interfacial Effects for Enhanced Hydrogen Evolution Reaction on MoS₂/WTe₂ Hybrid Structures. *Small* **2019**, *15*, 1900078.

(62) Hong, S. S.; Kundhikanjana, W.; Cha, J. J.; Lai, K.; Kong, D.; Meister, S.; Kelly, M. A.; Shen, Z.-X.; Cui, Y. Ultrathin Topological Insulator Bi₂Se₃ Nanoribbons Exfoliated by Atomic Force Microscopy. *Nano Lett.* **2010**, *10*, 3118–3122.



JACS Au
AN OPEN ACCESS JOURNAL OF THE AMERICAN CHEMICAL SOCIETY



Editor-in-Chief
Prof. Christopher W. Jones
Georgia Institute of Technology, USA

Open for Submissions 

pubs.acs.org/jacsau  ACS Publications
Most Trusted. Most Cited. Most Read.